Monthly Notices
of the
ROYAL ASTRONOMICAL SOCIETY

MNRAS **445,** 2825–2835 (2014) doi:10.1093/mnras/stu1955

Redshift-space distortions from the cross-correlation of photometric populations

Jacobo Asorey,★ Martin Crocce and Enrique Gaztañaga

Institut de Ciències de l'Espai (ICE, IEEC/CSIC), E-08193 Bellaterra (Barcelona), Spain

Accepted 2014 September 17. Received 2014 August 10; in original form 2013 May 20

ABSTRACT

Several papers have recently highlighted the possibility of measuring redshift-space distortions from angular auto-correlations of galaxies in photometric redshift bins. In this work, we extend this idea to include as observables the cross-correlations between redshift bins, as an additional way of measuring radial information. We show that this extra information allows us to reduce the recovered error in the growth rate index γ by a factor of $\sim$2. Although the final error in γ depends on the bias and the mean photometric accuracy of the galaxy sample, the improvement from adding cross-correlations is robust in different settings. Another factor of 2–3 improvement in the determination of γ can be achieved by considering two galaxy populations over the same photometric sky area but with different biases. This additional gain is shown to be much larger than the one from the same populations when observed over different areas of the sky (with twice the combined area). The total improvement of $\sim$5 implies that a photometric survey such as Dark Energy Survey should be able to recover γ at the 5–10 per cent from the angular clustering in linear scales of two different tracers. It can also constrain the evolution of $f(z) \times \sigma_8(z)$ in few bins beyond $z \sim 0.8$–0.9 at the 10–15 per cent level per bin, compatible with recent constrains from lower z spectroscopic surveys. We also show how further improvement can be achieved by reducing the photometric redshift error.

Key words: cosmological parameters – large-scale structure of the Universe.

1 INTRODUCTION

Our understanding of the local Universe and the way it evolved from small perturbations has been reshaped over the past decades with the successful completion of vast observational campaigns for cosmic microwave background fluctuations, large-scale structure and SNIa distances. Yet several still open issues arose from these studies, the most important of which is probably the late-time-accelerated expansion of the Universe.

Hence, many other cosmic surveys are ongoing or planned for the near future to address these questions with a set of precision measurements never achieved before. Several photometric surveys stand out among these, such as the Dark Energy Survey (DES),[1] the Panoramic Survey Telescope and Rapid Response System (PanStarrs),[2] the Physics of the Accelerating Universe survey (PAU)[3] and the future Large Synoptic Survey Telescope[4] or the imaging component of the ESA/*Euclid*[5] satellite.

Redshift-space distortions (RSD; Kaiser 1987; Hamilton 1998) can be used to understand the (linear) growth of structures, which provides a direct path to study the origin of cosmic acceleration. On large scales, RSD arises from the coherent velocities of galaxies and reveals how perturbations grow in time. Typically, this method requires measuring of galaxy clustering in three dimensions (3D) in order to sample directions parallel and transverse to the line of sight where the effect is maximized or cancels out completely (see e.g. Okumura et al. 2008; Cabré & Gaztañaga 2009; Guzzo et al. 2009; Blake et al. 2011; Reid et al. 2012; Kazin et al. 2013 and references therein).

Over the past few years, it has been however shown that the effect of RSD is also present, albeit with a smaller contribution, in the angular (2D) clustering of photometric galaxy samples if they are selected in photometric redshift bins, see for instance (Nock, Percival & Ross 2010; Crocce, Cabré, & Gaztañaga 2011a; Ross et al. 2011). This concrete idea has been already applied to data using a sample of photometric Luminous Red Galaxy (LRG; see Blake et al. 2007; Padmanabhan et al. 2007; Crocce et al. 2011b; Thomas, Abdalla & Lahav 2011).

Yet all the previous studies focused on the angular clustering from a set of measurements of auto-correlation in one or more redshift bins. In turn, cross-correlations have been proposed and mostly used to test for different systematics and to calibrate redshift distributions (see for instance Newman 2008; Thomas et al. 2011; Benjamin et al. 2013).

Hence, the goal of this paper is, on the one hand, to extend these analysis to include also the cross-correlations between redshift bins

★E-mail: asorey@ieec.uab.es

[1] www.darkenergysurvey.org
[2] pan-starrs.ifa.hawaii.edu
[3] www.pausurvey.org
[4] www.lsst.org
[5] www.euclid-imaging.net

in order to account for some radial information. This is motivated by the recent findings of Bonvin & Durrer (2011), Montanari & Durrer (2012), Asorey et al. (2012) who show how a tomographic (2D) study involving auto- and cross-correlations can yield similar constrains on cosmological parameters as a full spatial (3D) study. It is also important because a 2D formalism can naturally combine RSD with weak lensing (Cai & Bernstein 2012; Gaztañaga et al. 2012; de Putter, Doré & Takada 2013; Kirk et al. 2013). This is particularly relevant to discriminate between different models of modify gravity and general relativity (GR) by breaking the degeneracies between expansion history and growth of structure.

On the other hand, we will also investigate the improvements brought by considering two different populations (and their cross-correlations) in the likelihood analysis for the growth rate. This is motivated by the fact that for the spectroscopic analysis, the combination of different samples tracing the same underlying matter fluctuations can be used to decrease sampling variance and improve considerably the constrains in growth of structure (McDonald & Seljak 2009; White, Song & Percival 2009; Gil-Marín et al. 2010).

This paper is organized as follows. In Section 2, we lay out the methodology, including the analytical tools, the definition of the different samples and surveys and the likelihood analysis. In Section 3, we present our result, and in Section 4 our conclusions.

2 METHODOLOGY

Our goal is to study the effect of RSD in angular clustering, especially its usefulness to derive constrains on the growth of structure at large scales. We study angular clustering using auto- and cross- correlations between redshift bins. The inclusion of cross-correlations between different radial shells allow us to include the radial modes that account for scales comparable to the bin separation. On the other hand, the angular spectra of each redshift shell includes information mainly from transverse modes.

With the idea of a potential sample variance mitigation in the analysis, we also consider the correlation between the angular clustering of different tracers of matter, considering them either independent (i.e. each tracer in a different patch of the sky) or correlated (same sky).

Throughout this paper, we use CAMB_SOURCES[6] (Lewis, Challinor & Lasenby 2000; Lewis & Challinor. 2007; Challinor & Lewis 2011), including cross-correlations between radial bins and the correlations between different populations. Let us note that we use the exact C_ℓ computation in CAMB_SOURCES, because in angular clustering the imprint of redshift distortions affect mainly the largest scales, which are not included when using the Limber approximation (Limber 1954; LoVerde & Afshordi 2008; Crocce et al. 2011a). Moreover, the Limber approximations does not account for clustering in adjacent redshift bins.

2.1 Fiducial survey and galaxy samples

We start by describing the fiducial photometric survey that we assume in our analysis (characterized by a redshift range and a survey area) and the different galaxy samples considered within that volume (characterized by the bias b, the accuracy of photometric redshift estimates σ_z and their redshift distribution).

Our fiducial survey is similar to the full DES, with an area coverage of one octant of the sky (i.e. $f_{\rm sky} = 1/8$) and a redshift range $0.4 < z < 1.4$. We characterize the redshift distribution of galaxies within this survey by

$$\frac{{\rm d}N_\alpha}{{\rm d}z{\rm d}\Omega} = N^\alpha_{\rm gal}\left(\frac{z}{0.5}\right)^2 {\rm e}^{-\left(\frac{z}{0.5}\right)^{1.5}}, \quad (1)$$

where $N^\alpha_{\rm gal}$ is a normalization related to the total number of galaxies of each population sample, denoted by α. We typically consider two types of sample populations, one with bias $b = 1$ and $\sigma_z = 0.05(1+z)$ (Pop1) and another with $b = 2$ and $\sigma_z = 0.03(1+z)$ (Pop2) Banerji et al. (2008), Ross et al. (2011). For simplicity, we consider the same redshift distribution for all samples with a fiducial comoving number density of $n(z = 0.9) = 0.023\,h^3\,{\rm Mpc}^{-3}$, unless otherwise stated. This value corresponds to a total of $\sim 3 \times 10^8$ galaxies within the survey redshift range and matches the nominal number galaxies expected to be targeted above the magnitude limit of DES ($i < 24$). For more details about DES specifications, we refer the reader to The Dark Energy Survey Collaboration (2005).

Table 1. The different redshift bin configurations considered in our paper, within a photometric redshift range of $0.4 < z < 1.4$. We show the total number of bins and their redshift width Δz (which evolves with redshift in the same manner as the photo-z).

Number of bins N_z	$\Delta z/(1+z)$
4	0.15
6	0.1
8	0.08
12	0.05
19	0.03

In Table 1, we show the different redshift binning schemes in which we divide our survey prior to study the clustering either with the auto-correlations or with the 2D tomography that also includes the cross-correlations between bins. Note that we consider consecutive bins with an evolving bin width with redshift, i.e. $\Delta z \propto (1+z)$, to match the photometric uncertainty which also assumes a linear evolution with redshift.

2.2 Angular power spectrum

In our analysis, we study angular clustering using the angular power spectrum of the projected overdensities in the space of spherical harmonics. The auto-correlation power spectrum at redshift bin i, for a single population, is given by

$$C^{ii}_\ell = \frac{2}{\pi}\int {\rm d}k\, k^2 P_0(k)\left(\Psi^i_l(k) + \Psi^{i,r}_l(k)\right)^2, \quad (2)$$

where

$$\Psi^i_\ell(k) = \int {\rm d}z\, \phi_i(z) b(z) D(z) j_\ell(kr(z)) \quad (3)$$

is the kernel function in real space and

$$\Psi^{i,r}_\ell(k) = \int {\rm d}z\, \phi_i(z) f(z) D(z) \left[\frac{2l^2+2l-1}{(2\ell+3)(2\ell-1)} j_\ell(kr) - \frac{\ell(\ell-1)}{(2\ell-1)(2\ell+1)} j_{\ell-2}(kr) - \frac{(\ell+1)(\ell+2)}{(2\ell+1)(2\ell+3)} j_{\ell+2}(kr)\right] \quad (4)$$

[6] camb.info/sources

should be added to Ψ_ℓ^i if we also include the linear Kaiser effect (Fisher, Scharf & Lahav 1994; Padmanabhan et al. 2007). In equations (3) and (4), $b(z)$ is the bias (assumed linear and deterministic), $D(z)$ is the linear growth factor and $f(z) \equiv \partial \ln D / \partial \ln a$ is the growth rate. Photo-z effects are included through the radial selection function $\phi(z)$, see below.

For the case of 1 population, there are N_z auto-correlation spectra, one per radial bin. Then, we add to our observables the $N_z(N_z - 1)/2$ cross-correlations between different redshift bins. These are given by

$$C_\ell^{ij} = \frac{2}{\pi} \int \mathrm{d}k\, k^2 P(k) \left(\Psi_\ell^i(k) + \Psi_\ell^{i,r}(k)\right) \left(\Psi_\ell^j(k) + \Psi_\ell^{j,r}(k)\right). \tag{5}$$

Therefore, we are considering $N_z(N_z + 1)/2$ observable angular power spectra when reconstructing clustering information from tomography using N_z bins, for a single tracer.

If we combine the analysis of two tracers, α and β, the angular power spectrum is given by

$$C_\ell^{i_\alpha j_\beta} = \frac{2}{\pi} \int \mathrm{d}k\, k^2 P(k) \left(\Psi_\ell^{i_\alpha}(k) + \Psi_\ell^{i_\alpha,r}(k)\right) \left(\Psi_\ell^{j_\beta}(k) + \Psi_\ell^{j_\beta,r}(k)\right), \tag{6}$$

where Ψ_ℓ^i and $\Psi_\ell^{i,r}$ characterize each galaxy sample through the radial selection function $\phi_i(z)$ and the bias $b(z)$ in expressions (3) and (4). We use the general notation where $C_\ell^{i_\alpha j_\beta}$ is the correlation between redshift bin i of population α with redshift bin j of population β. By definition,

$$C_\ell^{i_\alpha j_\beta} = C_\ell^{j_\beta i_\alpha} \tag{7}$$

$$C_\ell^{i_\alpha j_\beta} \neq C_\ell^{j_\alpha i_\beta} \quad \text{for } \alpha \neq \beta; i \neq j. \tag{8}$$

Then, the total number of observables is $2N_z(2N_z + 1)/2$ if we consider the same redshift bins configuration for both populations, in the case in which both are correlated.

2.2.1 *Radial selection functions*

The radial selection functions ϕ_i in equations (2), (5) and (6) encode the probability to include a galaxy in the given redshift bin. Therefore, they are the product of the corresponding galaxy redshift distribution and a window function that depends on selection characteristics (e.g. binning strategy),

$$\phi_i^\alpha(z) = \frac{\mathrm{d}N_\alpha}{\mathrm{d}z} W_i(z), \tag{9}$$

where $\mathrm{d}N_\alpha/\mathrm{d}z$ is given by equation (1). We include the fact that we are working with photo-z by using the following window function:

$$W_i(z) = \int \mathrm{d}z_\mathrm{p} P(z|z_\mathrm{p}) W_i^{ph}(z_\mathrm{p}), \tag{10}$$

where z_p is the photometric redshift and $P(z|z_\mathrm{p})$ is the probability of the true redshift to be z if the photometric estimate is z_p. For our work, we assume a top-hat selection $W_i^{ph}(z_\mathrm{p})$ in photometric redshift and that $P(z|z_\mathrm{p})$ is Gaussian with standard deviation σ_z. This leads to

$$\phi_i^\alpha(z) \propto \frac{\mathrm{d}N_\alpha}{\mathrm{d}z} \left(\mathrm{erf}\left[\frac{z_{\mathrm{p,max}} - z}{\sqrt{2}\sigma_z^\alpha}\right] - \mathrm{erf}\left[\frac{z_{\mathrm{p,min}} - z}{\sqrt{2}\sigma_z^\alpha}\right]\right), \tag{11}$$

where $z_{\mathrm{p,\,min}}$ and $z_{\mathrm{p,\,max}}$ are the (photometric) limits of each redshift bin considered and σ_z^α is the photometric redshift error of the given population α at the corresponding redshift.

2.2.2 *Covariance matrix of angular power spectra*

We assume that the overdensity field is given by a Gaussian distribution and therefore, the covariance between correlation $C_\ell^{i_\alpha j_\beta}$ and correlation $C_\ell^{p_\alpha q_\beta}$ is given by

$$\mathrm{Cov}_{\ell,(i_\alpha j_\beta)(p_\mu q_\nu)} = \frac{C_\ell^{\mathrm{obs},i_\alpha p_\mu} C_\ell^{\mathrm{obs},j_\beta q_\nu} + C_\ell^{\mathrm{obs},i_\alpha q_\nu} C_\ell^{\mathrm{obs},j_\beta p_\mu}}{N(l)}, \tag{12}$$

where $N(\ell) = (2\ell + 1)\Delta\ell f_\mathrm{sky}$ is the number of transverse modes at a given ℓ provided with a bin width $\Delta\ell$. We set $\Delta\ell = 2/f_\mathrm{sky}$, the typically chosen value to make Cov block-diagonal (Cabré et al. 2007; Crocce et al. 2011a). In this case, bins in ℓ are not correlated between them.

Therefore, for each ℓ bin, we define a matrix with $2N_z(2N_z + 1)/2$ rows, where N_z is the number of redshift bins, taking into account the covariances and cross-covariances of auto- and cross-correlations between each population and among them. In order to include observational noise, we add to the auto-correlations of each population in equation (12) a shot noise term

$$C_\ell^{\mathrm{obs},i_\alpha j_\beta} = C_\ell^{i_\alpha j_\beta} + \delta_{i_\alpha j_\beta} \frac{1}{\frac{N_\mathrm{gal}(j_\beta)}{\Delta\Omega}} \tag{13}$$

that depends on the number of galaxies per unit solid angle included in each radial bin. We define the χ assuming the observed power spectrum C_ℓ^obs corresponds to our fiducial cosmological model discussed in Section 2.3, while we call C_ℓ^mod the one corresponding to the cosmology being tested

$$\chi^2 = \sum_\ell \left(C_\ell^\mathrm{obs} - C_\ell^\mathrm{mod}\right)^\dagger \mathrm{Cov}_\ell^{-1} \left(C_\ell^\mathrm{obs} - C_\ell^\mathrm{mod}\right). \tag{14}$$

2.3 Cosmological model and growth history

Throughout the analyses, we assume the underlying cosmological model to be a flat Λ cold dark matter (ΛCDM) with cosmological parameters $w = -1$, $h = 0.7$, $n_\mathrm{s} = 0.95$, $\Omega_\mathrm{m} = 0.25$, $\Omega_\mathrm{b} = 0.045$ and $\sigma_8 = 0.8$. These parameters specify the cosmic history as well as the linear spectrum of fluctuations P_0. In turn, the growth rate can be well approximated by

$$f(z) \equiv \Omega_\mathrm{m}(z)^\gamma \tag{15}$$

and $\gamma = 0.545$ for ΛCDM. Consistently with this, we obtain the growth history as

$$D(z) \equiv \exp\left[-\int_0^z \frac{f(z)}{1+z} \mathrm{d}z\right] \tag{16}$$

(where D is normalized to unity today). The parameter γ is usually employed as an effective way of characterizing modified gravity models that share the same cosmic history as GR but different growth history (Linder 2005). Our fiducial model assumes the GR value $\gamma = 0.545$. In order to forecast the constrains on γ, we consider it as a free parameter independent of redshift.

With these ingredients, we do a mock likelihood sampling in which we assume that the theoretical values for the correlations at the fiducial value of the parameters corresponds to the best-fitting position. The likelihood is based on the χ^2 given in equation (14). In our case, we keep fixed all the parameters and only allow γ to

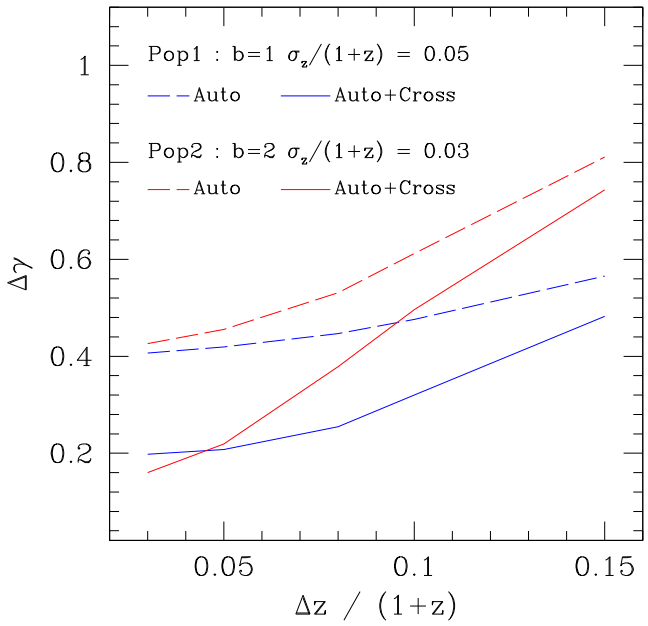

Figure 1. The gain from adding redshift-bins cross-correlations. Dashed lines show the expected 1σ constrains in γ from the combined analysis of angular auto-correlation in photo-z bins spanning $0.4 < z < 1.4$, as a function of the bin width $\Delta z/(1+z)$ (see Table 1 for the corresponding total number of bins). Different colours correspond to different populations with bias and σ_z as labelled. Solid lines show, for each population, the same study but also including all the cross-correlations between bins (and their complete covariance). For optimal bin widths $\Delta z \lesssim \sigma_z$, the gain from including cross-correlations is $\sim$2 or better.

vary, and then we estimate 68 per cent confidence limits of it. In the case in which we show constrains on $f\sigma_8$, we vary this quantity (that now depends on redshift, thus the number of fitting parameters is a function of the bin configuration), fixing the rest of parameters. The maximum ℓ considered in the analysis is $\ell_{\rm max} = r(\bar{z}_{\rm Survey})k_{\rm max} \sim 220$ for $k_{\rm max} = 0.1\,h\,{\rm Mpc}^{-1}$, while for the largest scales, we set $l_{\rm min} = 2$. We had to adapt CAMB_SOURCES in order to constrain γ or $f\sigma_8$ using the same technique described in the appendix A of Asorey et al. (2012).

3 RESULTS

In this section, we discuss the constrains on the growth index, γ defined in equation (15) as obtained for the different redshift bin configurations of Table 1. First of all, we study how well we can determine γ using different single galaxy populations but including as observables also the cross-correlation between bins (for a given single population). We also study how the constrains depend on the bias and in the photometric redshift accuracy of the different galaxy samples. Then, we study the precision achievable when one combines different tracers in the analysis and how this depends on bias, photo-z and in particular, the shot-noise level of the sample.

Lastly, we discuss the constrains that we obtain when looking into the more standard $f(z)\sigma_8(z)$ as a function of redshift, and consider auto- and cross-correlations of one or two galaxy samples.

3.1 RSD with a single photometric population

Let us first consider the constrains on the growth index using single photometric populations. Fig. 1 shows the 1σ errors expected on γ from a combined analysis of all the consecutive photometric redshift bins in the redshift range $0.4 < z < 1.4$ as a function of the bin width (i.e. each of the configurations detailed in Table 1).[7]

In red we show the constrains on γ corresponding to an LRG-type sample, with bias $b = 2$ and a photometric redshift $\sigma_z/(1+z) = 0.03$ (Pop2). Blue lines correspond to an unbiased population with $\sigma_z/(1+z) = 0.05$ (Pop1).

Dashed lines correspond to the case in which we only use the auto-correlations in each redshift bin while solid lines corresponds to the full 2D analysis that includes all the cross-correlations in our vector of observables. Recall that in the first case the cross-correlations are included in the covariance matrix of the auto-correlations (but not as observables). We see that constrains from a full 2D analysis, including auto- and cross-correlations are a factor $\sim$2 or more better than those from using only auto-correlations.

From Fig. 1, it is clear that in all cases the bin configuration can be optimized, with the best results obtained when $\Delta z \sim \sigma_z$. In addition, there is a competing effect between σ_z and bias. For broad bins ($\Delta z \gg \sigma_z$), the photo-z of the populations is masked in the projection and the bias dominates the γ constrains. Smaller bias gives more relevance to RSD and better γ constrains. As one decreases the bin width, the population with better photo-z (typically the brighter, with higher bias), denoted Pop2, allows a more detailed account of radial modes improving the derived errors on γ more rapidly than Pop1 until they become slightly better. This optimization is possible until one eventually reaches bin sizes comparable to the corresponding photo-z (what sets an 'effective' width) and the constrains flatten out.

In Fig. 2, we study in more detail the dependence of constrains with respect to galaxy bias b and photo-z accuracy. In the top panel of Fig. 2, we show standard deviation of the growth index, $\Delta\gamma$, fixing the sample bias to $b = 1$ and allowing two values for photo-z accuracy. Red line represents a sample in which $\sigma_z/(1+z) = 0.05$ while blue line has an error of $\sigma_z/(1+z) = 0.03$. In both cases, the constrain flattens once $\Delta z \sim \sigma_z$ and the optimal error improves roughly linearly with σ_z. The dependence on the linear galaxy bias, b, is shown in the bottom panel of Fig. 2 (for fixed σ_z). We see that the constrains degrade almost linearly with increasing bias (see also Ross et al. 2011). As discussed before, this is because the lower the bias the larger the relative impact of RSD, which results in better constraints on γ.

In summary, we have shown that using the whole 2D tomography (auto+cross-correlations) allows considerable more precise measurements of γ, a factor of 2 or better once the bin width is optimal for the given sample. Hence in what follows, we concentrate in full tomographic analysis.

3.2 RSD with two photometric populations

We now turn to an analysis combining two galaxy populations as two different tracers of matter. In Fig. 3, we compare the constrains from single tracers with respect to the combination of both. As before, the populations used in the comparison correspond to $b = 1$ and $\sigma_z/(1+z) = 0.05$ (Pop 1) and a population with $b = 2$ and $\sigma_z/(1+z) = 0.03$ (Pop 2). Their respective constrains in γ are the dashed red and blue lines (same as solid lines in Fig. 1).

If we combine both tracers and their cross-correlation in the same analysis, we obtain the constrains given by black solid line, notably

[7] Note that different redshift bins can be strongly correlated depending on bin width and photo-z. We do include this covariance.

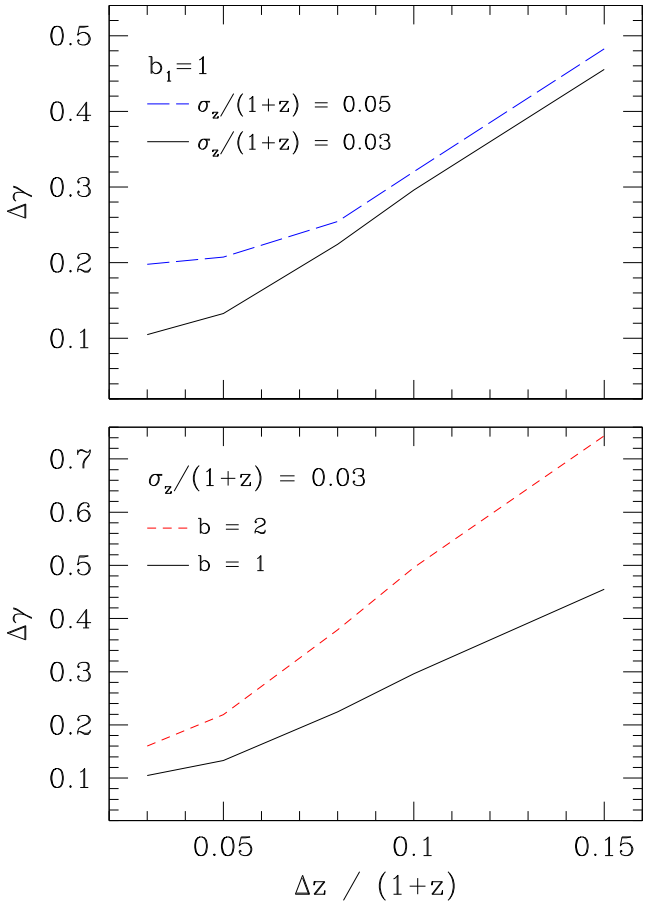

Figure 2. Dependence on photo-z (top panel) and bias (bottom panel) for a one-population constrains in γ, as a function of bin width (same as in Fig. 1). The panels show that lower b and/or lower σ_z yields better constrains in γ. This is hence a competing interplay because lower b would correspond to a fainter sample with typically worse photometric errors. The dependence on bias seems however slightly stronger.

a factor of 2–3 better compared to the optimal single population configuration.

In order to understand how much of this gain is due to 'sample variance cancellation', in analogy to the idea put forward in McDonald & Seljak (2009), we also considered combining the two samples assuming that they are located in different parts of the sky (and hence un-correlated). We call this case Pop1+Pop2 in Fig. 3 (solid green line). In such scenario, the total volume sampled is the sum of the volumes sampled by each population (in our case, two times the full volume of DES). This explains the gain with respect to the single population analysis. None the less, the 'same sky' case Pop1 × Pop2 (where cosmic variance is sampled twice) still yields better constrains, a factor of ∼1.5–2, even though the area has not increased w.r.t. Pop1 or Pop2 alone.

In all, the total gain of a full 2D study with two populations (including all auto- and cross-correlations in the range $0.4 < z < 1.4$) w.r.t. the more standard analysis with a single population and only the auto-correlations in redshift bins (dashed lines of Fig. 1) can reach a factor of ∼5.

As a next step, we show how the combined analysis of two tracers depends on the relative difference on the bias and photo-z errors of the populations. In Fig. 4, we keep Pop1 fix (with $b = 1$ and $\sigma_z/(1 + z) = 0.05$) and we vary the bias of Pop2 from $b = 2$ (LRG-type bias) to $b = 3$ (galaxy clustering like). We

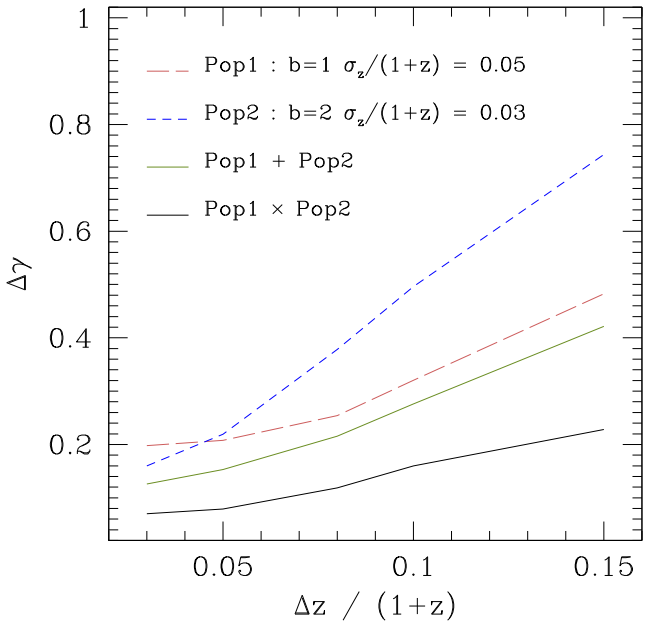

Figure 3. The gain from combining galaxy populations: comparison of the 68 per cent standard deviations in the growth index from single population analysis (dashed lines) with respect to the combined analysis of these two populations over the same field (black solid), using all the angular auto- and cross-correlations. Remarkably, the combination yields errors at least two times better than any of the single population cases. The solid green line corresponds to the combination of the two samples assuming that they are independent (i.e. from different parts of the sky). As shown, the combination of correlated populations (same sky) yield stronger constrains than any other case.

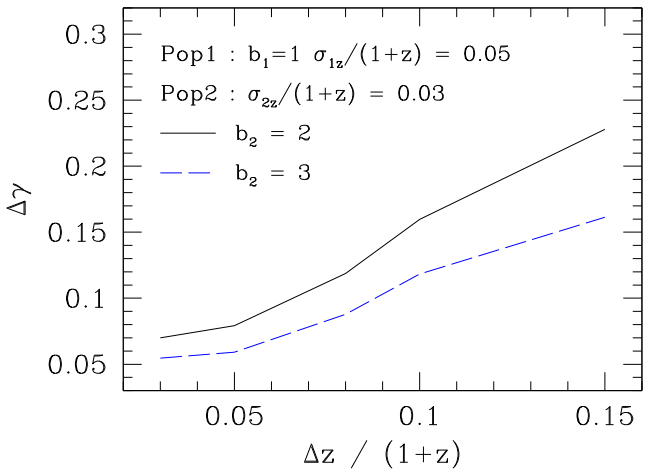

Figure 4. Dependence on bias. Increasing the bias difference between the samples improves the constrains on γ. The solid black line corresponds to the combination Pop1 × Pop2 of a highly biased sample such as LRGs (Pop2) with an unbiased one (Pop1), while the blue dashed to cluster-like bias tracer as Population 2.

keep $\sigma_z/(1 + z) = 0.03$ fixed for Pop2. As expected, increasing the bias difference between the samples improves the constrains on γ in a roughly linear way.

If we now have an unbiased tracer and a highly biased one with $b = 3$, while both tracers have the same $\sigma_z/(1 + z) = 0.03$, we obtain constrains given by the black line in Fig. 5. Those constrains are better than the case in which the unbiased galaxies photo-z is

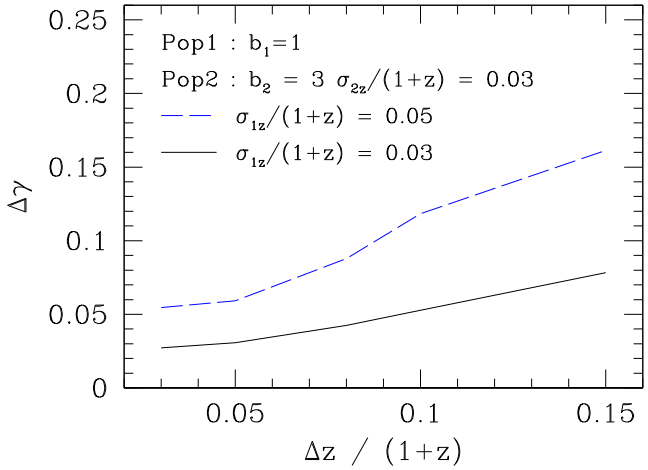

Figure 5. Dependence on photometric redshift error. Similar to Fig. 4 but now changing the photo-z of the unbiased sample (Pop1) for a fixed second population. The error on γ depend roughly linear with $\sigma_z/(1+z)$ for optimal bin widths.

worse, $\sigma_z/(1+z) = 0.05$ (given by the dashed blue line). Therefore, if we determine photometric redshifts of the unbiased galaxies with higher accuracy, we will be able to measure the growth rate with higher precision.

One caveat so far is that we have always assumed that biases are perfectly known (bias fixed). Hence, in the top panel of Fig. 6 we show how the constrains on γ change if we instead consider them as free parameters and marginalize over. We see that the difference is very small, in particular once the bin configuration is optimal. The reason for this is clear from the bottom panel that shows the relative error obtained for the bias of each sample in the bias free case. Because the bias is so well determined (sub-percent), the marginalization over them does not impact the error on γ.

3.2.1 *The impact of photo-z uncertainties*

The constrains on growth of structure presented in this paper rely to a good extent on cross-correlations between redshift bins, in turn largely determined by the overlap of the corresponding redshift distributions. So far, we have assumed a perfect knowledge of these distributions, given by equation (11). However, in a more realistic scenario, the distribution of photometric errors, and hence redshift distributions, will be known only up to some uncertainty. In this section, we investigate the impact of such uncertainties in the constraining power on growth rate by marginalizing over redshift distributions.

For concreteness, we focus in a case with only two redshift bins with $z_{\rm mean} = \{0.78, 0.96\}$ and width $\Delta z/(1+z) = 0.1$). In our framework, redshift distributions are characterized by a width, given by σ_z in equation (11), and set of minimum and maximum values for the photometric top-hat selection that determine the mean redshift $z_{\rm mean} = (z_{\rm p,\,min} + z_{\rm p,\,max})/2$. Thus, to marginalize over miss-estimations of photometric errors, the 'width' of $n(z)$, we vary σ_z. To marginalize over the 'mean redshift' of $n(z)$, we shift both $z_{\rm p,\,min}$ and $z_{\rm p,\,max}$ by the same amount. This procedure automatically changes either the width or the location of the underlying redshift distribution. Effectively, it also marginalizes over the amount of bin-overlap. In what follows, we do not put priors on any parameter.

Fig. 7 shows the 1σ contours of the growth rate index γ, the mean redshift of the second bin and the width of the photometric error at this bin for the bright population with $b = 2$ and $\sigma_z/(1+z_{\rm mean}) = 0.03$ (Pop 2). For this first case, we have chosen to set $z^{\rm bin1}_{\rm p,max} = z^{\rm bin2}_{\rm p,min}$ as we marginalized over mean redshift of bin 2. This means that we are also changing the width and location of the redshift distribution of bin 1 (while the amount of bin-overlap is set by the nuisance variable $\sigma_z^{\rm bin2}$). From Fig. 7, we find that marginalizing over $z_{\rm mean}$ and σ_z increases the best-fitting bin width above the fiducial value by 10 per cent but it does not bias the recovered growth rate index (neither the mean redshift). The error on γ increases by about 10 per cent when marginalizing over the $z_{\rm mean}$ and σ_z of bin 2, compared with the case with fixed $z_{\rm mean}$ and σ_z (represented by dashed lines in Fig. 7). In turn, the marginalization shows that σ_z and $z_{\rm mean}$ are slightly correlated (bottom-right panel of Fig. 7). We performed the same marginalization for the population with $b = 1$ and $\sigma_z/(1+z) = 0.05$ (Pop 1), finding similar conclusions (γ is recovered unbiased, with an error 14 per cent worse).

We also considered what happens if we do not keep both bins sharing the same boundary in photo-z space. In this case, the redshift distribution of bin 1 is kept totally fixed through marginalization of $n^{\rm bin2}(z)$ and the bin-overlap is changed by both $z_{\rm mean}$ and σ_z of bin 2. In this case, we find a smaller correlation between $z_{\rm mean}$ and σ_z

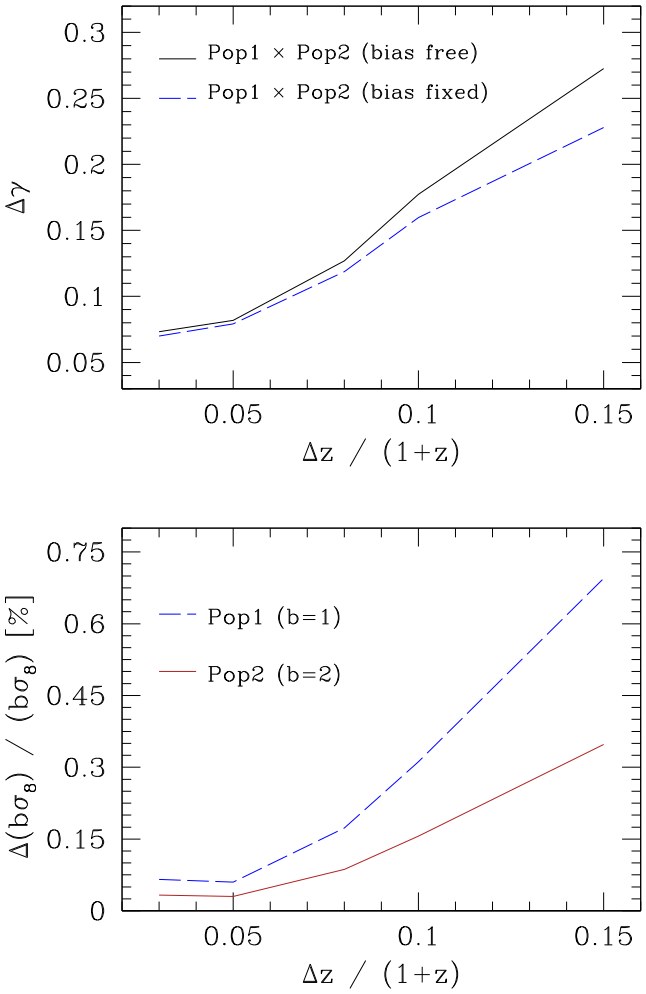

Figure 6. Bias free case: if the biases of the samples are free parameters to marginalize over, we find that constrains on γ degrade only slightly compared with the bias fixed case. In particular for the thinner redshift bins configurations. This is because biases are determined with relative errors smaller than 1 per cent (bottom panel).

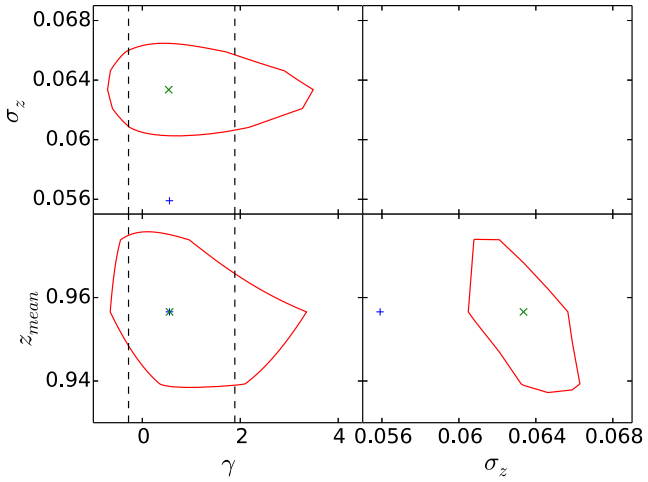

Figure 7. The impact of photo-z uncertainties on growth rate measurements. We considered a case with only two redshift bins, with fiducial $z_{\rm mean} = \{0.78, 0.96\}$ for a population with $b = 2$ and $\sigma_z/(1+z) = 0.03$ where the location ($z_{\rm mean}$) and width (σ_z) of the redshift distribution of the second bin are free parameters (in addition to γ). The figure shows the 68 per cent confidence regions for γ, $z_{\rm mean}$ and σ_z. Black dashed lines enclose the 1σ region when γ is the only free parameter. Blue '+' markers correspond to fiducial values while green 'x markers correspond to the best-fitting value after marginalizing over the remaining parameter. The marginalized error in γ increases by 10 per cent with respect to perfectly known redshift distributions (dashed lines). In turn, the best-fitting γ is unbiased (see text for further cases).

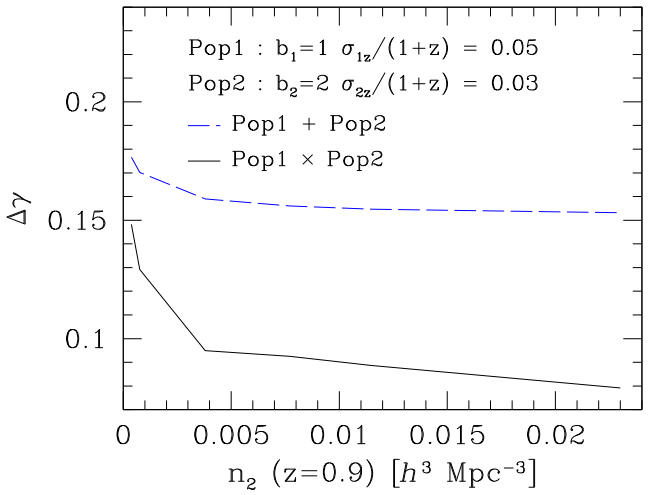

Figure 8. The impact of shot noise: we consider the combined analysis of two populations in a redshift bin configuration of $\Delta_z/(1+z) = 0.05$ and show how constrains on γ depend on the (shot) noise level of the more biased population (typically the brighter, less abundant sample). Constrains are almost un-affected unless the density drops by an order of magnitude or more compared to the one of Pop1 ($n_2 = 0.023\,h^3\,{\rm Mpc}^{-3}$).

and also a smaller marginalized error on $z_{\rm mean}$. The marginalized error on γ increases by 9 per cent when considering Pop1 and only 6 per cent for Pop2, while the best-fitting value is always recovered un-biased.

A full analysis on how to optimize and marginalize the photo-z uncertainties using more realistic photometric errors is beyond the scope of this paper. But the results presented in this section, and Fig. 7, indicate that it is possible to account for such uncertainties without a major loss in constraining power on growth rate measurements.

3.2.2 *The impact of shot-noise*

One strong limitation when it comes to implementing the 'multiple tracers' technique in real spectroscopic data is the need to have all the galaxy samples well above the shot-noise limit (at the same time as having the largest possible bias difference), see for instance Gil-Marín et al. (2010). This is cumbersome because spectroscopic data are typically sampled at a rate only slightly above the shot-noise (to maximize the area) and for pre-determined galaxy samples (e.g LRGs, CMASS). In a photometric survey, these aspects change radically because there is no pre-selection (beyond some flux limits) and the number of sampled galaxies is typically very large (at the expense of course of poor redshift resolution). Therefore, it is interesting to investigate if the overall density of the samples have any impact in our results.

Fig. 8 shows the constrain in γ for the combination of two samples, one unbiased population with $\sigma_z/(1+z) = 0.05$ and a population with $b = 2$ and $\sigma_z/(1+z) = 0.03$. We keep the number density for the unbiased population as $n(z = 0.9) = 1.8 \times 10^{-2}\,h^3{\rm Mpc}^3$ while we vary the number density of the second (typically brighter) sample.[8] The solid black line corresponds to the case in which both populations are correlated (same sky) and the dashed blue line to different areas. In both scenarios, we see that decreasing the number density of the second population does not impact the error on γ unless one degrades it by an order of magnitude or more (below $n(z = 0.9) \sim 3.0 \cdot 10^{-3}$). Above this value, the error is mostly controlled by the tracer with lower bias.

3.2.3 *Marginalizing over power spectrum shape*

In the analysis presented so far, we have assumed a perfect knowledge on the shape of the matter power spectrum and hence of the underlying cosmological parameters. However, it is important to explore possible degeneracies between the parameter we base on for RSD, namely γ, and other cosmological ones. While we leave a full exploration of degeneracies for a follow-up paper, we now study the impact of varying the shape of the power spectrum in addition to γ. We do this by considering the matter density $\Omega_{\rm m}$ as a nuisance parameter to marginalize over. By doing so, we are mostly studying the effect of the matter power spectrum shape in the analysis.

For concreteness, we focused on the binning configuration with $\Delta z/(1+z) = 0.1$ (6 bins). Fig. 9 shows the contour plots of the posterior distribution in the $\Omega_{\rm m} - \gamma$ for Pop1 (unbiased with bad photo-z), Pop2 (biased with good photo-z) and Pop1$\times$ Pop2. We find that there are no significant degeneracies and $\Omega_{\rm m}$ is determined with quite good precision.

Then, if we marginalize over $\Omega_{\rm m}$, we see that the errors on γ degrade a 16 per cent for an unbiased population, a 35 per cent for the biased one while the effect when we cross-correlate both populations is only a 6 per cent worse error on γ. Therefore, the conclusions obtained in previous sections are still valid, even if we allow the shape of the matter power spectrum to change.

[8] Note that we assume the same shape for $N(z)$ as given in equation (1) but we vary the overall normalization, which we characterize by the comoving number density at $z = 0.9$.

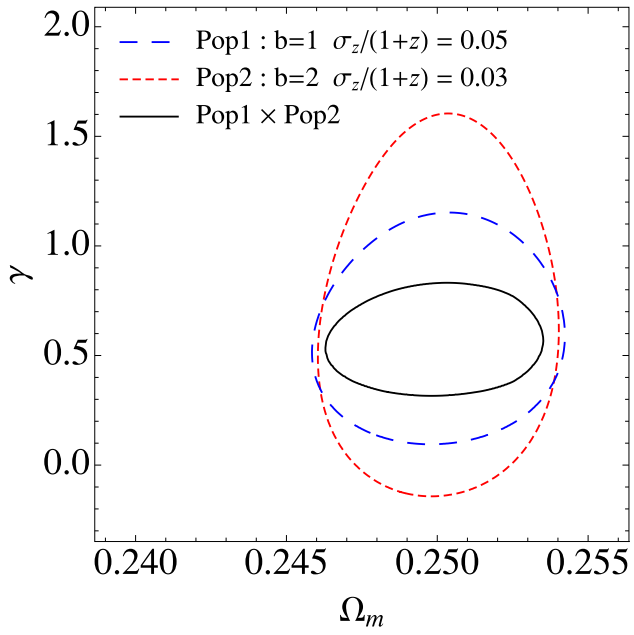

Figure 9. Marginalizing over the shape of $P(k)$: Contour plot of the posterior joint distribution when we consider both γ and $\Omega_{\rm m}$ as nuisance parameters. We find no significant degeneracies. The error on γ degrade 35 per cent for Pop1, 16 per cent for Pop2 and only 6 per cent for Pop1×Pop2. These results corresponds to a combined analysis of 6 bins with $\Delta z/(1+z) = 0.1$.

3.3 Constraining the redshift evolution of the growth rate of structure

So far, we have used the combined analysis of all the redshift bins to constrain one global parameter, namely the growth rate index γ in equation (15). We now turn into constraining $f(z)\sigma_8(z)$ itself, as a function of redshift. We use a redshift bin configuration given by $\Delta z/(1+z) = 0.1$, in the photometric range $0.4 < z < 1.4$. This configuration consist of six bins, and hence we fit $f(z)\sigma_8(z)$ evaluated at the mean of these bins. These $f\sigma_8$ values are of course correlated, and we include the proper covariance among the measurements (i.e. we do a global fit to the six values simultaneously).

In the left-hand panel of Fig. 10, we focus on the gain from adding cross-correlations among the bins, and show the constrain on $f\sigma_8$ for a single unbiased population with photometric redshift of $\sigma_z = 0.05$ (Pop 1, in blue) and also for a single tracer with bias $b = 2$ and $\sigma_z = 0.03$ (Pop 2, in red). Dashed lines corresponds to using only auto-correlations and solid to including also all the redshift bins cross-correlations to the observables. The trend for the errors when we only use auto-correlations are similar to the ones observed in fig. 8 of Ross et al. (2011). Although in detail we are using different widths for our redshift bins, and we use C_ℓ while they used angular correlation functions, $w(\theta)$.

As in Section 3.1, there is a gain from the addition of cross-correlations, which is now split across the bins (i.e. 20–30 per cent for Pop1 in each of the six bins, and a bit less for Pop2).

In turn, the right-hand panel of Fig. 10 focuses in the gain from combining the two tracers (and using both auto- and cross-correlations among redshift bins, as in Section 3.2). Here, the solid lines correspond to the single population cases discussed above, while the black short-dashed line to the combined analysis assuming that these populations are correlated (same sky). For completeness, the dashed green line is the result when these two samples are assumed independent. Again, there is a factor of ∼2.5 to be gained by combining galaxy samples as opposed to only the unbiased sample.

If we compare our predictions to measurements from spectroscopic surveys like VIPERS (de la Torre et al. 2013) with constrains $f\sigma_8(z = 0.8) = 0.47 \pm 0.08$ or WiggleZ (Blake et al. 2011) where $f\sigma_8(z = 0.76) = 0.38 \pm 0.04$, we find that DES can achieve the same level of errors (∼15 per cent) in determining the growth of

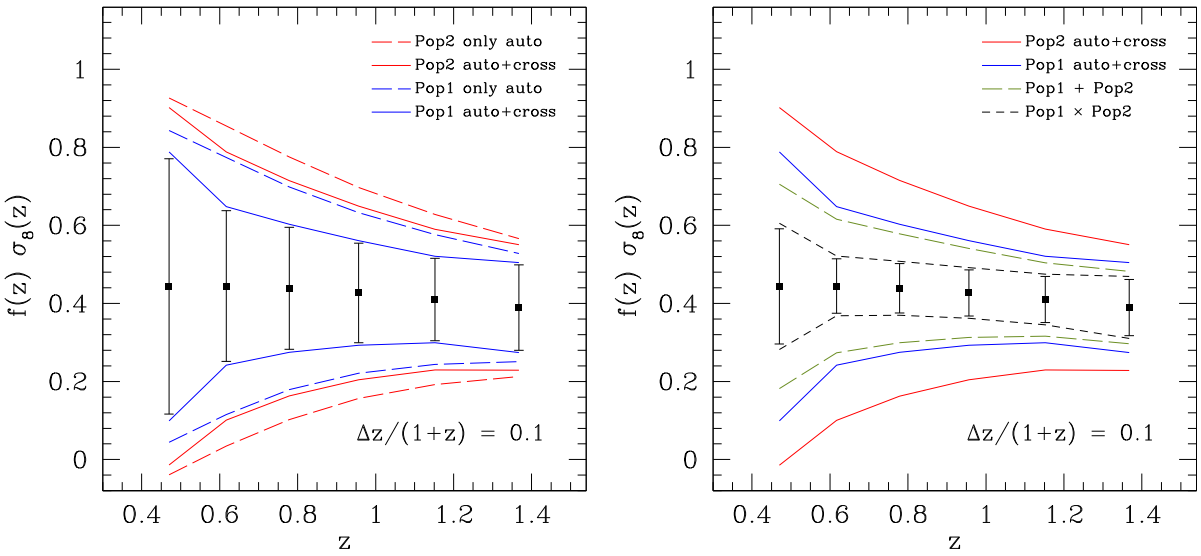

Figure 10. Constrains on $f\sigma_8$: derived at different redshift bins, for a bin configuration of $\Delta z/(1+z) = 0.1$. The left-hand panel focuses on one population only fits, and the gain from using auto+cross-correlations among all redshift bins as observables instead of just the auto-correlations. The right-hand panel stresses instead the gain from combining two populations (through their auto- and cross-correlations) either in different patches of the sky (Pop1+Pop2) or the same (Pop1×Pop2). In all cases, Pop1 refers to a galaxy population with $b = 1$ and $\sigma_z/(1+z) = 0.05$ and Pop2 to $b = 2$ and $\sigma_z/(1+z) = 0.03$. The covariance among the derived errors on $f(z) \times \sigma_8(z)$ is taken into account in the fit. Our results show that by using RSD with two tracers a DES-like photometric survey can place ∼15 per cent constrains in the evolution of $f\sigma_8$ for several bins in $z \gtrsim 0.8$ (with errors almost uncorrelated between bins, see text for details).

structure but extending the constrains beyond redshift of unity. This is quite unique and interesting as there is, to our knowledge, no other spectroscopic survey expected to provide such measurements in the medium term future (before ESA/*Euclid* or DESI).

3.3.1 Impact of unknown redshift distributions

In this section, we investigate the consequences of not having a perfect knowledge of the redshift distributions used to project the 3D clustering into tomographic bins. For concreteness, we do this by investigating how the error on $f\sigma_8$ resulting from a single bin at $z = 1.15$ change when we also vary the assumed underlying redshift distribution (within the binning configuration of $\Delta z/(1+z) = 0.1$). We note that in doing this we consider the full covariance with adjacent bins while the explored parameter space consist of three values of $f(z)\sigma_8(z)$ (at $z = 1.05, 1.15, 1.36$) and either the mean or the width of $N(z)$ for the central bin at $z = 1.15$.

We first concentrated in marginalized over the mean redshift of the assumed $N(z)$ for the central bin assuming a flat prior of 3 per cent around $z_{\rm mean} = 1.15$. We have repeated this for all the cases explored in Fig. 10, namely we consider populations 1 and 2 individually and then the same sky and different sky combinations of both populations. We have not found significant changes with respect to the results in previous sections finding differences smaller than 1 per cent for the cases with individual populations and less than 5 per cent for the case in which we combine the two populations.

Then, we marginalize over photometric errors and we find differences smaller than 1 per cent in the recovered constrains in $f(z)\sigma_8(z)$ with respect to the case in which we assume perfect knowledge of the redshift distributions. For concreteness, we did this cross-check for the case Pop1×Pop2 in last two redshift bins shown in Fig. 10.

3.4 The case of high-photometric accuracy

In the previous sections, we have focused in galaxy surveys with broad-band (BB) photometry for which the typical photometric error achieved is of the order of 0.1 depending on galaxy sample and redshift.[9] We now turn to narrow-band (NB) photometric surveys such as the ongoing PAU or J-PAS Surveys (Benitez et al. 2009; Castander et al. 2012; Gaztañaga et al. 2012; Taylor et al. 2014). These surveys are characterized by a combination of tens of NB filters (∼100Å) and few standard BB in the optical range. In the concrete case of PAU, the NB filters are 40 in total ranging from ∼4400 to ∼8600Å that will perform as a low-resolution spectrograph. With the current survey strategy, it will obtain accurate photometric redshifts for galaxies down to $i_{AB} \sim 22.5$ for which the typical redshift accuracy will be $\simeq 0.003(1+z)$ (or $10h^{-1}$ Mpc). This scenario then resembles quite closely a purely spectroscopic survey (Asorey et al. 2012). However, the expected density of this sample is ∼10 000 galaxies per deg^2, much denser than any spectroscopic surveys to the same depth.

We do not aim here at giving a forecast for PAU but rather at investigating the issue of combining samples with high-photometric accuracy. Hence, we will assume the same overall redshift distribution as in Section 2.1 but consider only a total 50×10^6 galaxies within 5000 deg^2. This is in broad agreement with PAU specifications (see Castander et al. 2012; Gaztañaga et al. 2012 for further details).

[9] We assumed 0.03 − 0.05 (1+z).

Table 2. Error in the growth rate γ from a combination of 21 narrow bins in the range $0.94 < z < 1.06$. The four top entries correspond to a Survey with BB filters: Pop1-BB assumes $b = 1$ and $\sigma_z/(1+z) = 0.05$ ('main sample') while Pop2-BB has $b = 2$ and $\sigma_z/(1+z) = 0.03$ ('LRG sample'). The four bottom entries correspond to a Survey with NB filters. Here, Pop1 and Pop2 have the same bias as the BB case but much precise photo-z, both with $\sigma_z/(1+z) = 0.003$.

Population	b	$\sigma_z/(1+z)$	Auto	Auto + Cross
Broad Band (BB)				
Pop1	1	0.05	0.809	0.564
Pop2	2	0.03	0.826	0.447
Pop1 × Pop2	–	–	–	0.35
Pop1 + Pop2	–	–	–	0.36
Narrow Band (NB)				
Pop1	1	0.003	0.047	0.027
Pop2	2	0.003	0.088	0.040
Pop1 × Pop2	–	–	–	0.016
Pop1 + Pop2	–	–	–	0.023

We again study two populations, one corresponding to the main sample with bias $b = 1$ and another to the LRG sample with $b = 2$, both with a very good photometric accuracy of $\sigma_z/(1+z) = 0.003$. We consider a set of 21 narrow redshift bins of width $\Delta z = 0.003(1+z)$ concentrated in $0.94 < z < 1.06$ (hence we are only looking at a portion of the survey redshift range).

The error on γ are given in Table 2, for both the new NB and the BB samples discussed previously. For a single population, this table shows that a factor of ∼10 better σ_z yields a factor of ∼10 gain in constraining power. The improvement in γ seems to increase linear with the improvement in σ_z.

After combining the two populations, we see that the errors in γ for the BB case is similar if samples cover the same region of sky (Pop1 × Pop2) or different regions (Pop1 + Pop2). This is because the redshift range considered ($0.94 < z < 1.06$) is too narrow compared to σ_z and the cosmic variance cancellation cannot take place. Instead, for the NB surveys, we find a 43 per cent improvement for the case Pop1 × Pop2 with respect to Pop1 + Pop2. For the same sky case, the final error is $\Delta\gamma \simeq 0.0163 \times (5000\,{\rm deg}^2/{\rm Area})^{1/2}$, in such a way that even a moderate survey of 250 deg^2 could achieve $\Delta\gamma \sim 0.07$. In that same narrow redshift range, DES yields an error five times worse with 20 times better area (but note that in the case of small areas, we could be limited by the $\ell_{\rm min}$, the largest scales available).

4 CONCLUSIONS

We have studied how measurement of RSD in wide field photometric surveys produce constrains on the growth of structure, in the linear regime. We focused in survey specifications similar to those of the ongoing DES or PanSTARRS, that is, covering about 1/8 of sky up to $z \sim 1.4$, and targeting galaxy samples with photometric redshift accuracies of $0.03 - 0.05(1+z)$ (and hundreds of million galaxies prior to sample selection). We also show results for ongoing photometric surveys, such as PAU and J-PAS, that have a much better photometric accuracy.

First, we have found that for a single population we can reduce the errors in half by including all the cross-correlations between radial shells in the analysis. This is because one includes large scale radial information that was missed when only considering the

auto-correlations of each bin. The final constraining power depends on the details of the population under consideration, in particular the bias and the photometric accuracy. Less bias gives more relative importance to RSD in the clustering amplitudes. In turn, better photo-z allows for narrower binning in the analysis and more radial information. We find that the γ constrains depend roughly linearly in both bias or σ_z. This means that for 10 times better photo-z errors, such as in PAU, we can improve by 10 the cosmological constrains.

Typically less bias implies a fainter sample, with worse photo-z, therefore these quantities compete in determining the optimal sample. Furthermore, we find that optimal constrains are achieved for bin configurations such that $\Delta z \sim \sigma_z$. Although the optimal errors depend on the details of the galaxy sample and binning strategy, the gains from adding cross-correlations are very robust in front of these variations.

In order to avoid sample variance, we have also considered what happens if we combine the measurement of RSD using two different tracers. This is motivated by the idea put forward in McDonald & Seljak (2009) for the case of spectroscopic (hence 3D) redshift surveys, where the over-sampling of (radial + transverse) modes allows a much better precision in growth rate constrains, as long as samples are in the low shot-noise limit. Combining auto and cross angular correlations in redshift bins, we find that if we assume that both tracers are independent, which corresponds to samples from different regions on the sky, the constrains on the growth of structure parameters improve a 30–50 per cent (due to the fact that one has doubled the area). Remarkably, if we consider that the populations are not independent, i.e. they trace the same field region, we find an overall improvement of ∼2–3 with respect to single populations when constraining γ. This means that there is a large potential gain when sampling the same modes more than once.

Translating into actual constrains, this implies that a DES-like photometric survey should be able to measure the growth rate of structure γ to an accuracy of 5–10 per cent from the combination of two populations and all the auto+cross-correlations in the range $0.4 < z < 1.4$ (see Fig. 1). Even though these values correspond to a survey of 5000 deg^2 ($f_{\rm sky} = 0.125$) they should scale as $f_{\rm sky}^{-1/2}$ for a different area, given our assumptions for the covariance in equation (12).

In Fig. 8, we have shown that constrains weaken once one of the populations enter a shot-noise-dominated regime, as is typical of spectroscopic samples. However, one needs to dilute over 10 times the number densities for a photometric survey, such as DES, for this to happen. Thus, as shown in Section 3.4, by improving on photo-z accuracy without much loss of completeness, a photometric sample can in fact outperform a diluted spectroscopic version with similar depth and area (see also Gaztañaga et al. 2012). In this paper, we focused on large angular scales where the approximation of linear and deterministic bias and linear RSD should hold (see for instance Crocce et al. 2011a). Although we set $\ell_{\rm max} \sim 200$, much of the constraining power in our results, given the typical size of our redshift bins, comes from larger scales, $\ell \lesssim 40$. Yet, a more realistic assessment of these aspects will need to resort to numerical simulations. We leave this for future work.

Lastly, we also investigated what constrains can be placed with this method in the evolution of the growth rate of structure, $f(z) \times \sigma_8(z)$. We found that binning two DES populations into six bins in the range $0.4 < z < 1.4$ yields constrains on $f(z) \times \sigma_8(z)$ of ∼15 per cent for each bin above $z \sim 0.6$. This is shown in Fig. 11. That case corresponded to bin widths larger than the photometric errors of the samples, which may not be optimal but yield constrains almost uncorrelated between bins ($\rho_{\rm ij} \sim -0.05$).[10] A narrower binning, $\Delta z/(1+z) = 0.05$ leads to better constrains per bin, $\Delta(f\sigma_8) \sim 10$ per cent, at the expense of more correlation between bins, $0.2 < \rho_{\rm ij} < 0.65$.

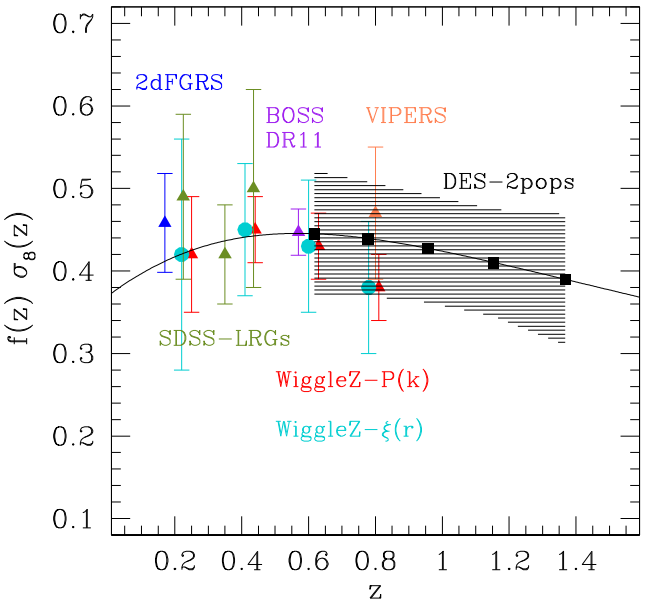

Figure 11. Combined constrains in the evolution of the growth rate of structure from spectroscopic data, 2dFGRS, SDSS-LRGs, Wiggle-Z, VIPERS and BOSS (see text for details), and forecasted for DES using two photometric populations (same as in Fig. 8). The addition of DES (shaded area) allows us to trace the growth rate of structure all the way to $z \sim 1.4$.

In addition to the DES forecast (shadowed region), we overplot in Fig. 11 current constrain from spectroscopic surveys, 2dFGRS (Percival et al. 2004), LRG's from SDSS (Tegmark et al. 2006; Cabré & Gaztañaga 2009), WiggleZ either from power spectrum (Blake et al. 2011) or correlation function (Contreras et al. 2013), and the recent VIPERS, (de la Torre et al. 2013) and BOSS results (Samushia et al. 2014). Note that these values are not expected to improve radically in the near future. This implies that DES will be able to add quite competitive constrains in a redshift regime unexplored otherwise with spectroscopic surveys (i.e. $z \gtrsim 1$), yielding a valuable redshift leverage for understanding the nature of dark energy and cosmic acceleration through the growth of structure.

ACKNOWLEDGEMENTS

We thank Pablo Fosalba, Will Percival and Ashley Ross for comments on the draft paper and helpful discussions. Funding for this project was partially provided by the Spanish Ministerio de Ciencia e Innovacion (MICINN), project AYA2009-13936, Consolider-Ingenio CSD2007- 00060, European Commission Marie Curie Initial Training Network CosmoComp (PITN-GA-2009-238356), research project 2009-SGR-1398 from Generalitat de Catalunya and the Ramon y Cajal MEC programme. JA was supported by the JAE program grant from the Spanish National Science Council (CSIC).

[10] For bins (i, j), we define the cross-correlation coefficient $\rho_{\rm ij}$ as $\rho_{\rm ij} = {\rm Cov_{ij}}/\sqrt{{\rm Cov_{ii}Cov_{jj}}}$ with ${\rm Cov_{ij}} = \langle (x - \langle x \rangle)_i (x - \langle x \rangle)_j \rangle$ and where x stands for $f \times \sigma_8$.

REFERENCES

Asorey J., Crocce M., Gaztañaga E., Lewis A., 2012, MNRAS, 427, 1891
Banerji M., Abdalla F. B., Lahav O., Lin H., 2008, MNRAS, 386, 1219
Benitez N. et al., 2009, ApJ, 691, 241
Benitez N. et al., 2013, MNRAS, 431, 1547
Blake C., Collister A., Bridle S., Lahav O., 2007, MNRAS, 374, 1527
Blake C. et al., 2011, MNRAS, 415, 2876
Bonvin C., Durrer R., 2011, Phys. Rev. D, 84, 063505
Cabré A., Gaztañaga E., 2009, MNRAS, 393, 1183
Cabré A., Fosalba P., Gaztañaga E., Manera M., 2007, MNRAS, 381, 1347
Cai Y. C., Bernstein G., 2012, MNRAS, 422, 1045
Castander F. J. et al., 2012, in McLean I. S., Ramsay S. K., Takami H., eds, Proc. SPIE, Vol. 8446, Ground-Based and Airborne Instrumentation for Astronomy IV. SPIE, Bellingham, p. 84466D
Challinor A., Lewis A., 2011, Phys. Rev. D, 84, 043516
Contreras C. et al., 2013, MNRAS, 430, 924
Crocce M., Cabré A., Gaztañaga E., 2011a, MNRAS, 414, 329
Crocce M., Gaztañaga E., Cabré A., Carnero A., Sánchez E., 2011b, MNRAS, 417, 2577
de la Torre S. et al., 2013, A&A, 557, A54
de Putter R., Doré O., Takada M., 2013, preprint (arXiv:1308.6070)
Fisher K. B., Scharf C. A., Lahav O., 1994, MNRAS, 266, 219
Gaztañaga E., Eriksen M., Crocce M., Castander F. J., Fosalba P., Marti P., Miquel R., Cabré A., 2012, MNRAS, 422, 2904
Gil-Marín H., Wagner C., Verde L., Jimenez R., Heavens A. F., 2010, MNRAS, 407, 772
Guzzo L. et al., 2008, Nature, 451, 541
Hamilton A. J. S., 1998, in Hamilton D., ed., Astrophysics and Space Science Library, Vol. 231, The Evolving Universe. Kluwer, Dordrecht, p. 185
Kaiser N., 1987, MNRAS, 227, 1
Kazin E. A. et al., 2013, MNRAS, 435, 64
Kirk D., Lahav O., Bridle S., Jouvel S., Abdalla F., Frieman J., 2013, preprint (arXiv:1307.8062)
Lewis A., Challinor A., 2007, Phys. Rev. D, 76, 083005
Lewis A., Challinor A., Lasenby A., 2000, ApJ, 538, 473
Limber D. N., 1954, ApJ, 119, 655
Linder E. V., 2005, Phys. Rev. D, 72, 043529
LoVerde M., Afshordi N., 2008, Phys. Rev. D, 78, 123506
McDonald P., Seljak U., 2009, J. Cosmol. Astropart. Phys., 0901, 007
Montanari F., Durrer R., 2012, Phys. Rev. D, 86, 063503
Newman J. A., 2008, ApJ, 684, 88
Nock K., Percival W. J., Ross A. J., 2010, MNRAS, 407, 520
Okumura T., Matsubara T., Eisenstein D. J., Kayo I., Hikage C., Szalay A. S., Schneider D. P., 2008, ApJ, 676, 889
Padmanabhan N. et al., 2007, MNRAS, 378, 852
Percival W. et al., 2004, MNRAS, 353, 1201
Reid B. et al., 2012, MNRAS, 426, 2719
Ross A. J., Percival W. J., Crocce M., Cabré A., Gaztañaga E., 2011, MNRAS, 415, 2193
Samushia L. et al., 2014, MNRAS, 439, 3504
Taylor K. et al., 2014, J. Astron. Instrum., 3, 1350010
Tegmark M. et al., 2006, Phys. Rev. D, 74, 123507
The Dark Energy Survey Collaboration, 2005, preprint (astro-ph/0510346)
Thomas S. A., Abdalla F. B., Lahav O., 2011, MNRAS, 412, 1669
White M., Song Y.-S., Percival W. J., 2009, MNRAS, 397, 1348

This paper has been typeset from a TEX/LATEX file prepared by the author.